

---

# **MODIS Observed Phytoplankton Dynamics in the Taiwan Strait: an Absorption-based Analysis**

**Shaoling Shang<sup>1</sup>, Qiang Dong<sup>2</sup>, Zhongping Lee<sup>2</sup>, Yonghong Li<sup>1</sup>,  
Yanshuang Xie<sup>1</sup>, Michael Behrenfeld<sup>3</sup>**

<sup>1</sup> State Key Laboratory of Marine Environmental Science, Xiamen University, Xiamen 361005, Fujian, China

<sup>2</sup> Geosystems Research Institute, Mississippi State University, MS 39529, USA

<sup>3</sup> Department of Botany and Plant Pathology, Oregon State University, OR 97333, USA

**Corresponding author: Shaoling Shang (s1shang@gmail.com)**

---

## 1    Abstract

2        This study used MODIS observed phytoplankton absorption coefficient at 443  
3        nm ( $Aph$ ) as a preferable index to characterize phytoplankton variability in optically  
4        complex waters.  $Aph$  derived from remote sensing reflectance ( $R_{rs}$ , both *in situ* and  
5        MODIS measured) with the Quasi-Analytical Algorithm (QAA) were evaluated by  
6        comparing them with match-up *in situ* measurements, collected in both oceanic and  
7        nearshore waters in the Taiwan Strait (TWS). For the data with matching spatial and  
8        temporal window, it was found that the average percentage error ( $\varepsilon$ ) between MODIS  
9        derived  $Aph$  and field measured  $Aph$  was 33.8% (N=30,  $Aph$  ranges from 0.012 to  
10        0.537 m<sup>-1</sup>), with a root mean square error in log space ( $RMSE_{log}$ ) of 0.226. By  
11        comparison,  $\varepsilon$  was 28.0% (N=88,  $RMSE_{log}$ =0.150) between  $Aph$  derived from  
12        ship-borne  $R_{rs}$  and  $Aph$  measured from water samples. However, values of  $\varepsilon$  as large  
13        as 135.6% (N=30,  $RMSE_{log}$ =0.383) were found between MODIS derived  
14        chlorophyll *a* (Chl, OC3M algorithm) and field measured Chl. Based on these  
15        evaluation results, we applied QAA to MODIS  $R_{rs}$  data in the period of 2003-2009 to  
16        derive climatological monthly mean  $Aph$  for the TWS. Three distinct features of  
17        phytoplankton dynamics were identified. First,  $Aph$  is low and the least variable in the  
18        Penghu Channel, where the South China Sea water enters the TWS. This region  
19        maintains slightly higher values in winter (~17% higher than that in the other seasons)  
20        due to surface nutrient entrainment under winter wind-driven vertical mixing. Second,  
21         $Aph$  is high and varies the most in the mainland nearshore water, with values peaking  
22        in summer (June-August) when river plumes and coastal upwelling enhance surface  
23        nutrient loads. Interannual variation of bloom intensity in Hanjiang River estuary in  
24        June is highly correlated with alongshore wind stress anomalies, as observed by  
25        QuikSCAT. The year of minimum and maximum bloom intensity is in the midst of an  
26        El Nino and a La Nina event, respectively. Third, a high  $Aph$  patch appears between  
27        April and September in the middle of the southern TWS, corresponding to high  
28        thermal frontal probabilities, as observed by MODIS. Our results support the use of  
29        satellite derived  $Aph$  for time series analyses of phytoplankton dynamics in coastal

---

30 ocean regions, whereas satellite Chl products derived empirically using spectral ratio  
31 of  $R_{rs}$  suffer from artifacts associated with non-biotic optically active materials.

32 **Keywords:** absorption coefficient, phytoplankton dynamics, MODIS, Taiwan  
33 Strait.

34 **1 Introduction**

35 While the concentration of phytoplankton pigments in the surface ocean reflect  
36 both variability in phytoplankton standing stocks and physiological state (e.g.  
37 Behrenfeld et al., 2005, Westberry et al., 2008), it has a clear impact on the optical  
38 properties of the water, allowing its relatively straight-forward retrieval from remote  
39 sensing measurements (e.g. Sathyendranath et al., 1994). The most common pigment  
40 product retrieved from ocean color remote sensing is chlorophyll *a* concentration (Chl,  
41 mg/m<sup>3</sup>; frequently used symbols throughout the manuscript are summarized in Table  
42 1). However, because of the optical complexity in nearshore waters (Carder et al.,  
43 1989; Zhang et al., 2006) and the simple spectral ratio approach (O'Reilly et al., 2000)  
44 used for the derivation of Chl, Chl product can be problematic in optically complex  
45 nearshore waters. Alternatively, analytical approaches (IOCCG, 2006) based on the  
46 radiative transfer theory have been developed to retrieve the spectral absorption  
47 coefficient of phytoplankton ( $a_{ph}$ , m<sup>-1</sup>). Using phytoplankton absorption, instead of  
48 Chl, as a superior metric of phytoplankton pigmentation is becoming increasingly  
49 accepted (e.g. Cullen, 1982; Marra et al., 2007), especially from the remote sensing  
50 point of view (Lee et al., 1996; Hirawake et al., 2011). This is because the direct  
51 controller of ocean color is the spectral absorption and scattering properties of the  
52 water media (e.g. Gordon et al., 1988) rather than pigment concentrations, although  
53 the variations of the latter will change pigment absorption in a non-stable fashion (e.g.  
54 Bricaud et al., 1998, Stuart et al., 1998). However, few studies based on *in situ*  
55 measurements exist to test whether  $a_{ph}$  can be derived from satellite ocean color data  
56 with less uncertainty than Chl. Such evidence is vital in order to confirm that  $a_{ph}$  can  
57 function as the preferable index for characterizing phytoplankton variability in the  
58 upper ocean. We here provide results conducted over the Taiwan Strait (TWS), a

---

59 shallow shelf channel that connects the South China Sea with the East China Sea (see  
60 Fig. 1), to demonstrate that 1) phytoplankton absorption can be retrieved more  
61 accurately than chlorophyll *a* in this optically complex ocean region from satellite  
62 observed ocean color and 2) changes of phytoplankton absorption capture  
63 phytoplankton dynamics in a vibrant and changing environment.

64 The TWS has complex hydrographic conditions determined by the relative  
65 influence of the South China Sea Warm Current (SCSWC) and the Kuroshio Branch  
66 Water (KBW), which are warm, saline, and oligotrophic, and the Zhe-Min Coastal  
67 Water (ZMCW), which is cold, fresh, and eutrophic, and varies seasonally in response  
68 to changes in the monsoonal wind (e.g. Jan et al., 2002). Several medium-sized rivers  
69 (e.g. Hanjiang and Jiulongjiang Rivers) are located on the western coast (mainland  
70 China) of the strait. Also along this coast, upwelling develops in summer, driven by  
71 the prevailing southwest monsoon which runs parallel to the coast due to Ekman  
72 transport (e.g. Hong et al., 2009). Different waters converge in a limited area with a  
73 shallow bank (Taiwan Bank), a ridge (Zhangyun Ridge), and deep channel (Penghu  
74 Channel), creating strong frontal phenomena (e.g. Chang et al., 2006; Li et al., 2006).

75 For this study, we first derived  $a_{ph}$  from remote sensing reflectance ( $R_{rs}$ ,  $sr^{-1}$ ) with  
76 the quasi-analytical bio-optical inversion algorithm (QAA, Lee et al., 2002; 2009). In  
77 addition to QAA, there are several algorithms available for the retrieval of absorption  
78 and backscattering coefficients from  $R_{rs}$  (IOCCG, 2006). Here we used QAA because  
79 of its transparency in the analytical inversion process and simplicity in  
80 implementation. We evaluated the  $R_{rs}$  derived  $a_{ph}$  by comparing it with match-up *in*  
81 *situ* measured  $a_{ph}$  collected in both oceanic and nearshore waters in the TWS. Finally  
82 we applied QAA to MODIS  $R_{rs}$  data for the period 2003-2009 to derive climatological  
83 monthly mean  $a_{ph}$  at 443 nm (also represented as *Aph* for brevity) and to evaluate  
84 spatio-temporal variation of the mean *Aph* in the TWS.

85 **2 Data and methods**

86 **2.1 Satellite data**

87 Aqua-MODIS daily Level-2 normalized water leaving radiance ( $nLw$ ,

---

88  $W \cdot m^{-2} \cdot nm^{-1} \cdot sr^{-1}$ , 2005 reprocessed version) data were obtained from the NASA  
89 Distributed Active Archive Center (<http://oceancolor.gsfc.nasa.gov/>) and were  
90 subsequently converted to  $R_{rs}$  via the ratio of  $nLw$  to extra-terrestrial solar irradiance,  
91  $F_0$  ( $W \cdot m^{-2} \cdot nm^{-1}$ ) (Gordon, 2005; also see  
92 [http://oceancolor.gsfc.nasa.gov/DOCS/RSR\\_tables.html](http://oceancolor.gsfc.nasa.gov/DOCS/RSR_tables.html)). Aqua-MODIS Level-2 Chl  
93 daily data during 2003-2009, which were derived by using the OC3M empirical  
94 algorithm (O'Reilly et al., 2000), were also obtained from the same source. These data  
95 were further processed into Level-3 products by using Mercator projection, which was  
96 implemented on SeaDAS ([http://seadas.gsfc.nasa.gov/doc/tutorial/sds\\_tut2.html](http://seadas.gsfc.nasa.gov/doc/tutorial/sds_tut2.html)). The  
97 spatial resolution of these data was 1 km by 1 km.

98 Daily wind field data were obtained from QuikScatterometer (QuikSCAT)  
99 observations from 2003 to 2009 (<http://podaac.jpl.nasa.gov>), with a spatial resolution  
100 of  $0.25^\circ$  by  $0.25^\circ$  (equivalent to  $\sim 25$  km by  $\sim 25$  km). Daily wind stress ( $T$ ,  $N/m^2$ ) was  
101 calculated from (Stewart, 2008):

$$102 \quad T = \rho_a C_D U_{10}^2 \quad (1)$$

103 where  $\rho_a = 1.3 \text{ kg/m}^3$  was the density of air,  $U_{10}$  (m/s) was wind speed at 10 meters  
104 (the QuiSCAT measurement), and  $C_D$  was the drag coefficient.  $C_D$  was calculated  
105 from Yelland and Taylor (1996) and Yelland et al. (1998). Wind stress vectors were  
106 further decomposed into alongshore (southwesterly) and cross-shore (northwesterly)  
107 components by applying a simple vector manipulation.

108 Aqua-MODIS sea surface temperature (SST,  $^\circ\text{C}$ ) monthly mean data (4 km by 4  
109 km resolution) during 2003-2009 were downloaded from  
110 <http://oceandata.sci.gsfc.nasa.gov/>. Based on this SST data, we derived a thermal  
111 frontal probability map for the TWS by following Wang et al. (2001). Briefly, we  
112 calculated the SST gradients in eight directions for each clear pixel and chose the  
113 average over the three absolute maxima as the horizontal gradient for this pixel. Only  
114 pixels whose gradients were equal to or greater than the threshold of  $0.5^\circ\text{C}$  per 4 km  
115 were regarded as frontal pixels. The frontal probability was then obtained by dividing

---

116 the number of times the pixel was frontal, by the accumulative number of times the  
117 pixel had a valid SST value.

118 **2.2 Calculation of mean and anomaly**

119 To address spatio-temporal variations of properties derived from satellite  
120 measurements, temporal and spatial means and anomalies were calculated for each  
121 property. These properties included the non-water absorption at 443 nm (total  
122 absorption coefficient without contribution from pure water;  $a_{t-w}(443)$ ,  $m^{-1}$ ) and  $Aph$   
123 from QAA\_v5, Chl from OC3M, and QuikSCAT derived alongshore component of  
124 wind stress.

125 For pixel  $i$  in month X year Y, the monthly mean of a property was obtained by  
126 adding up all the available daily values in the month and then dividing them by the  
127 number of days having valid values. The spatial mean of each property in month X  
128 year Y ( $\bar{P}_{x,y}$ ) was calculated by adding up all the available monthly mean values in  
129 the TWS area in the month and dividing them by the number of pixels having valid  
130 retrievals. The TWS area was defined as the ocean area between the China mainland  
131 coast or the 116.5°E longitude and the 122 °E, and between 22°N and 25.5°N (see Fig.  
132 1, the area enclosed by the dashed grey lines, the mainland coastline and the 122 °E).

133 For pixel  $i$  in month X, the climatological monthly mean of a property ( $\bar{P}_{i,x}$ ) was  
134 calculated by adding up all the monthly values for 2003-2009 and then dividing them  
135 by the number of years (=7). The spatial mean of each property in month X ( $\bar{P}_x$ ) was  
136 then calculated based on this climatological monthly mean dataset following the  
137 above mentioned procedure for calculation of  $\bar{P}_{x,y}$ .

138 The spatial anomaly of a property in pixel  $i$  month X was derived from  $\bar{P}_{i,x} - \bar{P}_x$ .  
139 The temporal anomaly of a property in month X year Y was calculated from  $\bar{P}_{x,y} -$   
140  $\bar{P}_x$ .

---

141 **2.3 *In situ* data**

142 **2.2.1 Remote sensing reflectance**

143 *In situ*  $R_{rs}$  was derived from measured (1) upwelling radiance ( $L_u$ ,  
144  $W \cdot m^{-2} \cdot nm^{-1} \cdot sr^{-1}$ ), (2) downwelling sky radiance ( $L_{sky}$ ,  $W \cdot m^{-2} \cdot nm^{-1} \cdot sr^{-1}$ ), and (3)  
145 radiance from a standard Spectralon reflectance plaque ( $L_{plaque}$ ,  $W \cdot m^{-2} \cdot nm^{-1} \cdot sr^{-1}$ ).  
146 The instrument used was the GER 1500 spectroradiometer (Spectra Vista Corporation,  
147 USA), which covers a spectral range of 350-1050 nm with a spectral resolution of 3  
148 nm. From these three components,  $R_{rs}$  was calculated as:

149 
$$R_{rs} = \rho(L_u - F \cdot L_{sky}) / (\pi \cdot L_{plaque}) - \Delta \quad (2)$$

150 where  $\rho$  is the reflectance (0.5) of the spectralon plaque with Lambertian  
151 characteristics and  $F$  is surface Fresnel reflectance (around 0.023 for the viewing  
152 geometry).  $\Delta$  ( $sr^{-1}$ ) accounts for the residual surface contribution (glint, etc.), which  
153 was determined either by assuming  $R_{rs}(750)=0$  (clear oceanic waters) or through  
154 iterative derivation according to optical models for coastal turbid waters as described  
155 in Lee et al. (2010).

156 **2.2.2 Field-measured absorption coefficients and chlorophyll *a***

157 Water samples for determination of absorption coefficients and Chl were  
158 collected from surface waters during 2003-2007 in the TWS. Sampling station depths  
159 ranged from ~10 m to ~400 m. Measurements of chromophoric dissolved organic  
160 matter (CDOM) absorption coefficient,  $a_g(m^{-1})$ , and Chl were performed according to  
161 the Ocean Optics Protocols Version 2.0 (Mitchell et al., 2000), and were detailed in  
162 Hong et al. (2005) and Du et al. (2010). Particulate absorption coefficient ( $a_p$ ,  $m^{-1}$ )  
163 was measured by the filter-pad technique (Kiefer and SooHoo, 1982) with a  
164 dual-beam PE Lambda 950 spectrophotometer equipped with an integrating sphere  
165 (150 mm in diameter) following a modified Transmittance–Reflectance (T-R) method  
166 (Tassan and Ferrari, 2002; Dong et al., 2008). This approach was used instead of the T  
167 method recommended in the NASA protocol (Mitchell et al., 2000) because some of  
168 the samples were collected nearshore. These samples were rich in highly scattered

---

169 non-pigmented particles. The standard T-method will thus cause an overestimate of  
170 sample absorption (Tassan and Ferrari, 1995). Detrital absorption ( $a_d$ ,  $m^{-1}$ ) was  
171 therefore obtained by repeating the modified T-R measurements on samples after  
172 pigment extraction by methanol (Kishino, 1985).  $a_{ph}$  was then calculated by  
173 subtracting  $a_d$  from  $a_p$ , and the combination of  $a_p$  and  $a_g$  yields an estimation of  $a_{t-w}$ .

174 Combining all the field studies, we collected 104 sets of *in situ* data, with each  
175 set including  $a_{t-w}$ ,  $a_{ph}$ ,  $a_d$ ,  $a_g$  and Chl. This *in situ* dataset covered a wide range of  
176 absorption properties, with  $a_{t-w}(443)$  ranging from 0.019 to 2.41  $m^{-1}$ , and the  
177  $a_{ph}(443)/a_{t-w}(443)$  ratio varying between 9%-86%.

178 Due to frequent cloud cover in the TWS, only 30 matching data pairs were  
179 achieved of *in situ* absorption and Chl data collected within  $\pm 24h$  of MODIS overpass  
180 (Fig. 1, circle symbols). By comparison, there were 88 sets of *in situ* absorption and  
181 Chl data having match-up *in situ*  $R_{rs}$  measurements (Fig. 1, cross symbols).

182 **3 Evaluation of  $R_{rs}$  derived absorption coefficients in the Taiwan Strait**

183  $R_{rs}$  from field measurements and MODIS were fed to QAA\_v5 (Lee et al., 2009),  
184 respectively, to derive two sets of  $a_{t-w}$  and  $a_{ph}$ . In order to evaluate the quality of  $R_{rs}$   
185 derived  $a_{ph}$ , we used the root mean square error both in linear scale ( $RMSE$ ) and in log  
186 scale ( $RMSE_{log}$ ), and averaged percentage error ( $\varepsilon$ ) as a measure to describe the  
187 similarity/difference between the field measured (f) and retrieved data sets (r):

188 
$$\varepsilon = \left( \frac{1}{n} \sum_{i=1}^n \left| \frac{r_i - f_i}{f_i} \right| \right) \times 100\% \quad (3)$$

189 
$$RMSE = \sqrt{\frac{1}{n} \sum_{i=1}^n (r_i - f_i)^2} \quad (4)$$

190 
$$RMSE_{log} = \sqrt{\frac{1}{n} \sum_{i=1}^n (\log(r_i) - \log(f_i))^2} \quad (5)$$

191 Results were given in Table 2. Fig. 2 (a & b) compares the derived and measured  $a_{t-w}$   
192 and  $a_{ph}$  values at 443 nm for the MODIS (the yellow square symbols) and the *in situ*  
193 (the blue circle symbols) data sets, respectively.

194 Averaged percentage error ( $\varepsilon$ ) and  $RMSE_{log}$  between *in situ* measured  $a_{ph}(412)$

---

195 and MODIS  $a_{ph}(412)$  were 36.1% and 0.252, respectively, for an  $a_{ph}(412)$  range of  
196 0.009–0.539 m<sup>-1</sup>. Similarly,  $\varepsilon$  was 33.8% and  $RMSE\_log$  was 0.226 for an  $a_{ph}(443)$   
197 range of 0.012–0.537 m<sup>-1</sup> (Table 2). These errors decreased when  $a_{ph}$  was derived  
198 from ship-borne  $R_{rs}$ . For example, the  $\varepsilon$  was 28.0% and the  $RMSE\_log$  was 0.150 for  
199 443 nm (Table 2). Such a difference was not surprising since additional uncertainties  
200 were introduced in satellite match-ups that were associated with imperfections in  
201 atmospheric correction over coastal water for the MODIS  $R_{rs}$  (Dong, 2010) and the  
202 spatio-temporal mismatch between satellite and field data (1 km<sup>2</sup> versus 1m<sup>2</sup>, and the  
203 temporal window of  $\pm 24$  h) . Nevertheless, these results were better than the global  
204 evaluation results reported in the IOCCG Report No.5 (IOCCG, 2006), which used  
205 the earliest version of QAA (Lee et al, 2002). In that report, no satellite  $R_{rs}$  derived  $a_{ph}$   
206 data were evaluated and the  $RMSE\_log$  between *in situ*  $R_{rs}$  derived  $a_{ph}(443)$  and field  
207 measured  $a_{ph}(443)$  was 0.321 (it was 0.150 in this study). A recent evaluation of  
208 SeaWiFS  $R_{rs}$  derived  $a_{ph}(443)$  using QAA at an European coastal site produced a  
209  $RMSE\_log$  of 0.21 ( Mélin et al., 2007), which was comparable to our results.

210 The difference between *in situ* measured Chl and match-up  $R_{rs}$  derived Chl (via  
211 OC3M) was much larger than found for *Aph* (Fig. 2c). Between *in situ* measured Chl  
212 and MODIS  $R_{rs}$  derived Chl, the  $\varepsilon$  was 135.6% and  $RMSE\_log$  was 0.383. Between *in*  
213 *situ* measured Chl and *in situ*  $R_{rs}$  derived Chl, the  $\varepsilon$  was 162.0% and  $RMSE\_log$  was  
214 0.429. This analysis of match-up uncertainties clearly indicated improved  
215 performance of  $R_{rs}$ -retrieved *Aph* over Chl in the TWS. One fundamental reason for  
216 such results is that  $R_{rs}$  is largely determined by the absorption and scattering  
217 properties of all the optically active materials in the water, of which phytoplankton is  
218 simply one of them (Mobley, 1994; IOCCG, 2006). Higher uncertainty associated  
219 with Chl is thus anticipated while trying to retrieve Chl by simple spectral ratio of  $R_{rs}$   
220 in marine waters where the contribution of non-phytoplankton components is  
221 significant (e.g., TWS).

---

222 **4 Comparison on the spatial patterns of MODIS  $a_{\text{ph}}(443)$ ,  $a_{\text{t-w}}(443)$  and Chl in**  
223 **the Taiwan Strait**

224 The above analysis of match-up uncertainties supports the use of  $R_{\text{rs}}$  derived  $Aph$   
225 as a preferable index (compared to Chl) to represent phytoplankton in the optically  
226 complex coastal water of the TWS. A time series of MODIS  $Aph$  for the TWS was  
227 thus derived by inputting daily MODIS  $R_{\text{rs}}$  into QAA\_v5. Climatological monthly  
228 mean  $Aph$  during 2003–2009 were then derived, along with  $a_{\text{t-w}}(443)$  from QAA\_v5  
229 and Chl from OC3M. Before using this multi-year monthly mean  $Aph$  dataset to  
230 address phytoplankton dynamics in the TWS, we further did a comparison on the  
231 spatial patterns of  $Aph$ ,  $a_{\text{t-w}}(443)$  and Chl for the entire TWS. This additional analysis  
232 was conducted to address a concern that the evaluation results shown in Section 3  
233 were merely a comparison of discrete match-up samples in the TWS and most of the  
234  $R_{\text{rs}}$  data used in the analysis were *in situ* measurements, rather than MODIS  
235 measurements. The spatial patterns of the three properties in the TWS were revealed  
236 by calculating their spatial anomalies and normalizing each to their respective spatial  
237 mean. The  $RMSD$  (root mean square deviation) between each pair of normalized  
238 spatial anomalies was calculated as:

239 
$$RMSD = \sqrt{\frac{1}{n} \sum_{i=1}^n \delta^2} \quad (6)$$

240 where  $\delta$  was the difference between each pair of normalized spatial anomalies, and  $n$   
241 was the pixel number (varies from 134000 to 148118, depending on percentage of  
242 cloud cover in each month). As shown in Fig. 3, the  $RMSD$  was larger between Chl  
243 and  $Aph$  (the grey bar) than between Chl and  $a_{\text{t-w}}(443)$  (the empty bar), especially  
244 during the cold season when the wind was strong and the water was relatively turbid  
245 due to sediment resuspension (Guo et al., 1991). This finding clearly indicates that the  
246 spatial pattern of empirically derived MODIS Chl was more similar to that of MODIS  
247  $a_{\text{t-w}}(443)$  than MODIS  $Aph$ . Thus, the empirical MODIS Chl product was registering  
248 the combined influence of phytoplankton pigments and other optically active  
249 materials (detritus and CDOM) in the TWS, similar as that found in the South Pacific

---

250 Gyre (Lee et al., 2010). Using analytically derived *Aph* from MODIS measurements  
251 to study phytoplankton dynamics is thus further justified.

252 **5 Spatio-temporal variation of MODIS *Aph* in the Taiwan Strait**

253 The monthly mean of each year and climatological monthly mean MODIS *Aph*  
254 dataset were used to analyze the spatio-temporal variations of *Aph* during 2003-2009.

255 First, the annual mean *Aph* and its standard deviation (STD) were derived from  
256 the climatological monthly mean MODIS *Aph*. The STD identifies a highly variable  
257 area located alongshore the China mainland, and an area showing low temporal  
258 variation located in the deepest zone of the TWS (i.e. the Penghu Channel), adjacent  
259 to the South China Sea (Fig. 4a).

260 To investigate further the seasonality of *Aph* in waters of low temporal variation,  
261 we chose a square in the Penghu Channel (right bottom of Fig. 4a) and derived its  
262 monthly time series. Although variations are weak, *Aph* slightly increases during  
263 December to March by about 17% over the mean level of *Aph* in the other months  
264 (Fig. 4b). This seasonal pattern with a winter maximum is similar to *in situ*  
265 observations of Chl, phytoplankton cell counts, and primary production at SEATS  
266 (18°N 116°E, South East Asian Time-series Study station, Tseng et al., 2005) and the  
267 entire South China Sea (Ning et al., 2004; Chen, 2005). This correspondence between  
268 seasonal cycles of phytoplankton pigment in the TWS and the South China Sea is not  
269 surprising since this part of the TWS is dominated by the SCSWC (Jan et al., 2002).  
270 Enhanced nitrate availability in winter due to enhanced wind-driven vertical mixing is  
271 thought to play a role in modulating phytoplankton dynamics in this water (Chen,  
272 2005), although photoacclimation and altered grazing pressure may also be important  
273 (Behrenfeld et al. 2005; Behrenfeld, 2010).

274 In contrast to the Penghu Channel water, *Aph* is highly variable alongshore the  
275 China mainland, influenced by inputs of the Jiulongjiang and Hanjiang Rivers (see  
276 locations in Fig. 1) and by upwelling in summer (Hong et al., 2009) and the Zhe-Min  
277 Coastal Water in winter (Jan et al., 2002). In the nearshore band west of the white line  
278 on Fig. 4a, *Aph* ranges from 0.048 m<sup>-1</sup> in March to 0.088 m<sup>-1</sup> in June (Fig. 4b).

---

279 Overall, *Aph* peaks in summer (June-August) at a value 64% higher than the  
280 minimum *Aph* observed in spring (March-May). Summer is the season of peak river  
281 flow, which accounts for 44% of the annual discharge (Sun et al., 2009; <http://bai->  
282 [ke.baidu.com/view/23372.html](http://baike.baidu.com/view/23372.html)). Summer is also the season of southwesterly wind,  
283 which drives coastal upwelling (Hong et al., 2009). Nearshore phytoplankton blooms,  
284 as indexed by the high *Aph* values, are thus supported by the availability of nutrients  
285 provided by both river plumes and upwelling.

286 A close-up view of this nearshore water in May-August (Fig. 5a) clearly  
287 demonstrates the combined impacts of river plumes and upwelling in summer. Out of  
288 each estuary, there is a tongue of high *Aph* (generally  $\geq 0.1 \text{ m}^{-1}$ ) advecting  
289 northeastward. This feature is most distinct in June (Fig. 5a). In the vicinity of  
290 Hanjiang River estuary (also nearby the Dongshan Island), a broad area of especially  
291 high *Aph* is found, relative to values for the Jiulongjiang River estuary. This  
292 difference is, in part, due to the volume of Hanjiang River annual flow at  $258 \times 10^9 \text{ m}^3$ ,  
293 which is ~80% higher than the Jiulongjiang River ( $142 \times 10^9 \text{ m}^3$ ) (Sun et al., 2009). In  
294 addition, a significant upwelling center is located in the vicinity of Dongshan Island  
295 (Hong et al., 2009). These combined factors (upwelling and stronger river plume)  
296 result in stronger blooms for the Hanjiang River estuary area.

297 To investigate the interannual variation of bloom intensity for such an upwelling  
298 enhanced bloom in the Hanjiang River estuary area, we used the monthly mean of  
299 each year *Aph* data to derive an annual areal bloom index (ABI). ABI was calculated  
300 as the sum of *Aph* in pixels having  $Aph \geq 0.1 \text{ m}^{-1}$  for all valid observations in a month  
301 (*Aph* of  $0.1 \text{ m}^{-1}$  corresponds to  $\sim 1.7 \text{ mg/m}^3 \text{ Chl}$  in the TWS (Dong, 2010)). The ABI  
302 within a square representing the Hanjiang River estuary (see location on the June  
303 image of Fig. 5a; its area is  $9400 \text{ km}^2$ ) in June of each year during 2003-2009 is  
304 shown in Fig. 5b (the empty circle), along with the percentage of valid pixels to  
305 retrieve the ABI (the grey bar), the alongshore wind stress anomaly (the solid circle),  
306 and the Multivariate ENSO Index (MEI,  
307 <http://www.cdc.noaa.gov/people/klaus.wolter/MEI/>) (the red and blue curve). The

---

308 ABI peaks in 2008 and is the lowest in 2004, and is well correlated with the  
309 alongshore wind stress anomaly ( $r^2=0.67$ ,  $n=7$ ). More positive alongshore wind stress  
310 anomalies correspond to stronger southwesterly winds, which drive enhanced  
311 upwelling, offshore advection of river plumes, and stronger phytoplankton blooms  
312 (and vice versa). However, the ABI in 2009 is  $152 \text{ m}^{-1}$ , even lower than the ABI in  
313  $2003 (776 \text{ m}^{-1})$ . The alongshore wind stress anomaly is positive in 2009 and negative  
314 in 2003, suggesting bloom favoring conditions in 2009 compared to 2003. This  
315 abnormally low number in 2009 is in part due to missing satellite data in the Hanjiang  
316 River estuary area owing to heavy cloud cover. In total, there are 7771 pixels in the  
317 square for ABI estimation. As the grey bar in Fig. 5b shows, during most of the year,  
318 more than 80% of the pixels in the square have valid retrievals; while in 2009, only 29%  
319 of the pixels had valid *Aph* data. Therefore, additional uncertainties of satellite data  
320 due to bad weather conditions must be noted, necessitating careful examination of the  
321 data. If we remove data from 2009 where ABI values are abnormally low in number,  
322 the  $r^2$  between ABI and the alongshore wind stress anomaly increases to 0.97 ( $n=6$ ).

323 Interestingly, variations of the ABI show coincidence with ENSO activities,  
324 illustrated by the match of the empty circles (ABI) and the red and blue curve (MEI)  
325 (Fig. 5b). Positive MEI (red curve) indicates occurrence of El Nino while negative  
326 MEI (blue curve) corresponds to La Nina. The year of the lowest ABI (2004) is in the  
327 midst of an El Nino event (2000-2005), and the year of the highest ABI (2008) is in  
328 the midst of a La Nina event (2007-2009). Such an ABI difference between El Nino  
329 and La Nina years might be more significant, if it is influenced by potential  
330 differences in cloud cover between El Nino and La Nina years, since 78% of the total  
331 pixels have valid retrievals in 2008 while the percentage of valid retrievals is as high  
332 as 86% in 2004 (see the grey bar in Fig. 5b). It has been acknowledged that the  
333 relationship between the Asian monsoon and ENSO is mutual but selectively  
334 interactive (e.g. Webster and Yang 1992). However, which factor is the underlying  
335 cause and which is the effect remain unclear (e.g. Kinter III, et al., 2002). Here we  
336 have observed a strong coastal bloom in 2008, when the southwest monsoon is the

---

337 strongest (during 2003-2009) and a La Nina event is occurring. We have also  
338 observed a weak bloom in 2004, when the southwest monsoon is the weakest (during  
339 2003-2009) and an El Nino event is at its mid-point. Further study of regional scale  
340 ecosystem variability should advance understanding of the monsoon-ENSO  
341 interaction.

342 Spatial anomalies of  $Aph$  also highlight a distinctly high  $Aph$  patch generally  
343 located in the middle of the southern TWS, appearing in the period of April to  
344 September (Fig. 6a). This patch is likely associated with (1) shelf break upwelling in  
345 the vicinity of the Taiwan Bank (Li et al, 2000), (2) island stirring around Penghu  
346 Islands (Simpson and Tett, 1986) and (3) upwelling associated with Zhangyun Ridge  
347 (Pi and Hu, 2010). Frontal probabilities derived from MODIS SST during 2003-2009  
348 are greater than 60% in the area corresponding to this  $Aph$  patch (Fig. 6b). Since  
349 vertical temperature gradients are smaller during cold seasons, these fronts can only  
350 be well developed in the surface water during warm seasons (April-September).  
351 Fronts provide powerful physical forcings to inject nutrients from deep water into the  
352 surface, thus facilitating phytoplankton growth.

353

## 354 6 Conclusion

355 The current study provided both an assessment of algorithm performance and a  
356 description of phytoplankton dynamics in the optically complex TWS. Based on our  
357 analysis of 104 *in situ* measurements in the TWS, we found that the QAA algorithm  
358 provided a satisfactory assessment of  $a_{ph}$  from both MODIS and ship borne  $R_{rs}$ . We  
359 further derived climatological monthly mean  $Aph$  (2003-2009) from MODIS  $R_{rs}$  with  
360 QAA and found a variety of seasonal patterns for  $Aph$  in the TWS. The most  
361 interesting result is that the phytoplankton bloom in the vicinity of Hanjiang River  
362 estuary, which is enhanced by upwelling in summer, shows an order of magnitude  
363 variation during 2003-2009. This interannual variability is highly correlated with  
364 alongshore wind stress anomalies and ENSO activities, and demonstrates ecological  
365 responses to changing in environmental forcings, documented here for the first time

---

366 by using satellite *Aph* data. This dynamics was not revealed when satellite Chl  
367 product was employed, as there are large uncertainties in the spectral-ratio derived  
368 Chl in nearshore waters (Zhang, 2006). It should be noted, however, that *Aph* is not a  
369 full reflection of variability in phytoplankton pigmentation because of the package  
370 effect (Bricaud et al., 1998), even though they are directly related to each other. Some  
371 uncertainties also remain in our satellite  $a_{ph}$  products due to issues with variable cloud  
372 cover that may introduce biases in our results, especially in winter. Repeated  
373 observations from multi-sensors and geostationary satellites may help resolve such  
374 problems in the future.

375

### 376 **Acknowledgements**

377 This work was supported jointly by the High-tech R & D program of China  
378 (#2008AA09Z108), NSF-China (#40976068), the National Basic Research Program  
379 of China (#2009CB421200 and 2009CB421201), the China Scholarship Council, and  
380 the Program of ITDU (#B07034). Support for M. Behrenfeld was provided through the  
381 National Aeronautics and Space Administration (#NNX08AF73A). We thank the  
382 crew of the R/V Yanping II, and J. Wu, X. Ma, X. Sui, W. Zhou, W. Wang, M. Yang,  
383 C. Du and G. Wei for their help in collecting *in situ* data and Drs. Allen Milligan and  
384 Toby Westberry for helpful discussions during our analysis.

385

### 386 **References**

387 Behrenfeld, M. J., Boss, E., Siegel, D. A., and Shea, D. M.: Carbon-based ocean productivity and  
388 phytoplankton physiology from space, *Global Biogeochem. Cy.*, 19, GB1006,  
389 doi:10.1029/2004GB002299, 2005.

390 Behrenfeld, M. J.: Abandoning Sverdrup's Critical Depth Hypothesis on phytoplankton blooms,  
391 *Ecology*, 91, 977-989, 2010.

392 Bricaud, A., Morel, A., Babin, M., Allali, K., and Claustre, H.: Variations of light absorption by  
393 suspended particles with chlorophyll a concentration in oceanic (case 1) waters: Analysis and  
394 implications for bio-optical models, *J. Geophys. Res.*, 103, 31033-31044, 1998.

---

395 Carder, K. L., Steward, R. G., Harvey, G. R., and Ortner, P. B.: Marine humic and fulvic acids:  
396       their effects on remote sensing of ocean chlorophyll, *Limnol. Oceanogr.*, 34, 68-81, 1989.

397 Carder, K. L., Chen, F. R., Lee, Z., Hawes, S. K., and Kamykowski, D.: Semianalytic  
398       Moderate-Resolution Imaging Spectrometer algorithms for chlorophyll a and absorption with  
399       bio-optical domains based on nitrate-depletion temperatures, *J. Geophys. Res.*, 104,  
400       5403-5421, 1999.

401 Chang, Y., Shimada, T., Lee, M. A., Lu, H. J., Sakaida, F., and Kawamura, H.: Wintertime sea  
402       surface temperature fronts in the Taiwan Strait, *Geophys. Res. Lett.*, 33, L23603,  
403       doi:10.1029/2006GL027415, 2006.

404 Chen, L.: Spatial and seasonal variations of nitrate-based new production and primary production  
405       in the South China Sea, *Deep-Sea. Res. Pt I*, 52, 319-340, 2005.

406 Cullen, J. J.: The deep chlorophyll maximum: Comparing vertical profiles of chlorophyll a, *Can. J.*  
407       *Fish. Aquat. Sci.*, 39, 791-803, 1982.

408 Dong, Q., Hong, H., Shang, S.: A new approach to correct for pathlength amplification in  
409       measurements of particulate spectral absorption by the quantitative filter technique, *Journal*  
410       *of Xiamen University (Natural Science)*, 47, 556-561, 2008 (In Chinese, with English  
411       abstract).

412 Dong, Q.: *Derivation of Phytoplankton Absorption Properties from Ocean Color and Its*  
413       *Application*, Ph. D., Xiamen University (China), 2010.

414 Du, C., Shang, S., Dong, Q., Hu, C., and Wu, J.: Characteristics of Chromophoric Dissolved  
415       Organic Matter in the nearshore waters of the western Taiwan Strait, *Estuar. Coast. Shelf. S.*,  
416       88, 350-356, 2010.

417 Gordon, H. R., Brown, O. B., Evans, R. H., Brown, J. W., Smith, R. C., Baker, K. S., and Clark, D.  
418       K.: A semianalytic radiance model of ocean color, *J. Geophys. Res.*, 93, 10909-10924, 1988.

419 Gordon, H. R.: Normalized water-leaving radiance: revisiting the influence of surface roughness,  
420       *Appl. Optics.*, 44, 241-248, 2005.

421 Guo, L., Hong, H., Chen, J., and Hong, L.: Distribution and variation of suspended matter in the  
422       southern Taiwan Strait, In: Hong, H., Minnan-taiwan bank fishing ground upwelling  
423       ecosystem study, 273-281, 1991 (In Chinese, with English abstract).

---

424 Hirawake, T., Takao, S., Horimoto, N., Ishimaru, T., Yamaguchi, Y., and Fukuchi, M.: A  
425 phytoplankton absorption-based primary productivity model for remote sensing in the  
426 Southern Ocean, *Polar Biology* (accepted).

427 Hong, H., Wu, J., Shang, S., and Hu, C.: Absorption and fluorescence of chromophoric dissolved  
428 organic matter in the Pearl River Estuary, *South China, Mar. Chem.*, 97, 78-89, 2005.

429 Hong, H., Zhang, C., Shang, S., Huang, B., Li, Y., Li, X., and Zhang, S.: Interannual variability of  
430 summer coastal upwelling in the Taiwan Strait, *Cont. Shelf. Res.*, 29 , 479-484, 2009.

431 Jan, S., Wang, J., Chern, C.S., and Chao, S.Y.: Seasonal variation of the circulation in the Taiwan  
432 Strait, *J. Marine. Syst.*, 35, 249-268, 2002.

433 Kiefer, D. A., and SoohHoo, J. B.: Spectral absorption by marine particles of coastal waters of  
434 Baja California, *Limnol. Oceanogr.*, 27, 492-499, 1982.

435 Kinter III, J., Miyakoda, K., and Yang, S.: Recent change in the connection from the Asian  
436 monsoon to ENSO, *J. Climate*, 15, 1203-1215, 2002.

437 Kishino, M., Takahashi, M., Okami, N., and Ichimura, S.: Estimation of the spectral absorption  
438 coefficients of phytoplankton in the sea, *B. Mar. Sci.*, 37, 634-642, 1985.

439 Lee, Z., Carder, K. L., Marra, J., Steward, R. G., and Perry, M. J.: Estimating primary production  
440 at depth from remote sensing, *Appl. Optics.*, 35(3), 463-474, 1996.

441 Lee, Z., Carder, K. L., and Arnone, R. A.: Deriving inherent optical properties from water color: a  
442 multiband quasi-analytical algorithm for optically deep waters, *Appl. Optics.*, 41, 5755-5772,  
443 2002.

444 Lee, Z.: Remote sensing of inherent optical properties: fundamentals, tests of algorithms, and  
445 applications, In: Stuart, V., International Ocean-Colour Coordinating Group, No. 5, IOCCG,  
446 Dartmouth, Canada, 2006.

447 Lee, Z., Carder, K. L, Arnone, R. A, and He, M.: Determination of primary spectral bands for  
448 remote sensing of aquatic environments, *Sensors*, 7, 3428-3441, 2007.

449 Lee, Z., Lubac, B., Werdell, J., and Arnone, R.: An update of the Quasi-Analytical Algorithm  
450 (QAA\_v5), [http://www.ioccg.org/groups/Software\\_OCA/QAA\\_v5.- pdf](http://www.ioccg.org/groups/Software_OCA/QAA_v5.- pdf), 2009.

451 Lee, Z., Ahn, Y., Mobley, C., and Arnone, R.: Removal of surface-reflected light for the  
452 measurement of remote-sensing reflectance from an above-surface platform, *Opt Express*,

---

453 18(25), 26313-26342, 2010.

454 Lee, Z., Shang, S., Hu, C., Lewis, M., Arnone, R., Li, Y., and Lubac, B.: Time series of  
455 bio-optical properties in a subtropical gyre: Implications for the evaluation of inter-annual  
456 trends of biogeochemical properties, *J. Geophys. Res.* 115, C09012,  
457 doi:10.1029/2009JC005865, 2010.

458 Li, C., Hu, J., Jan, S., Wei, Z., Fang, G. H., and Zheng, Q.: Winter-spring fronts in Taiwan Strait, *J.*  
459 *Geophys. Res.*, 111, C11S13, doi:10.1039/2005JC003203, 2007.

460 Li, L., Guo, X., and Wu, R.: Oceanic fronts in southern Taiwan Strait, *Journal of Oceanography in*  
461 *Taiwan Strait*, 19, 147-156, 2000 (In Chinese, with English abstract).

462 Maritorena, S., Siegel, D. A., and Peterson, A. R.: Optimization of a semianalytical ocean color  
463 model for global-scale applications, *Appl. Optics.*, 41, 2705-2714, 2002.

464 Marra, J., Trees, C. C., and O'Reilly, J.E.: Phytoplankton pigment absorption: A strong predictor  
465 of primary productivity in the surface ocean, *Deep-Sea. Res. Pt I*, 54, 155-163, 2007.

466 Mélin, F., Zibordi, G., and Berthon, J.F.: Assessment of satellite ocean color products at a coastal  
467 site, *Remote. Sens. Environ.*, 110, 192-215, 2007.

468 Mitchell, B. G., Bricaud, A., and Carder, K.: Determination of spectral absorption coefficients of  
469 particles, dissolved material and phytoplankton for discrete water samples, In: Fargion, G.S.  
470 and Mueller, J.L., *Ocean optics protocols for satellite ocean color sensor validation*, revision  
471 2, Greenbelt, Maryland: NASA Goddard Space Flight Space Center, 125-153, 2000.

472 Ning, X., Chai, F., Xue, H., Cai, Y., Liu, C., and Shi, J.: Physical-biological oceanographic  
473 coupling influencing phytoplankton and primary production in the South China Sea, *J.*  
474 *Geophys. Res.*, 109, C10005, doi:10.1029/2004JC002365, 2004.

475 O'Reilly, J. E., Maritorena, S., Siegel, D., and O'Brien, M. C.: Ocean color chlorophyll a  
476 algorithms for SeaWiFS, OC2, and OC4: version 4, In: Hooker, S. B. and Firestone, E. R.,  
477 SeaWiFS postlaunch technical report series, volume 11, SeaWiFS postlaunch calibration and  
478 validation analyses, part 3, Greenbelt, Maryland: NASA Goddard Space Flight Center, 9-23,  
479 2000.

480 Pi, Q. and Hu, J.: Analysis of sea surface temperature fronts in the Taiwan Strait and its adjacent  
481 area using an advanced edge detection method, *Science China, Earth Science*, 53, 1008-1016,

---

482 2010.

483 Sathyendranath, S., Hoge, F. E., Platt, T., and Swift, R. N.: Detection of phytoplankton pigments  
484 from ocean color: Improved algorithms, *Appl. Optics.*, 33, 1081-1089, 1994.

485 Shang, S., Zhang, C., Hong, H., Liu, Q., Wong, G.T.F., Hu, C., and Huang, B.: Hydrographic and  
486 biological changes in the Taiwan Strait during the 1997-1998 El Nino winter, *Geophys. Res.*  
487 *Lett.*, 32, L11601, doi:10.1029/2005GL022578, 2005.

488 Simpson, J. H. and Tett, P.: Island steering effects on phytoplankton growth, In: Bowman, J.,  
489 Yentsch, M., and Peterson, W. T., *Lecture notes on coastal and estuarine studies*, Berlin,  
490 41-76, 1986.

491 Stewart, R.H.. *Introduction to physical oceanography*. Department of Oceanography, Texas A &  
492 M University. 2008

493 Stuart, V., Sathyendranath, S., Platt, T., Maass, H., and Irwin, B.: Pigments and species  
494 composition of natural phytoplankton populations: effect on the absorption spectra, *J.*  
495 *Plankton Res.*, 20, 187-217, 1998.

496 Sun, B., Zhou, G., Wei, H., Liu, Z., and Zeng, D.: The flux of river active material flowing into  
497 the sea: Preliminary achievements, *Earth Science Frontiers*, 16, 361-368, 2009 (In Chinese,  
498 with English abstract).

499 Tassan, S. and Ferrari, G. M.: A sensitivity analysis of the 'Transmittance-Reflectance' method for  
500 measuring light absorption by aquatic particles, *J. Plankton. Res.*, 24, 757-774, 2002.

501 Tseng, C. M., Wong, G. T. F., Lin, I. I., Wu, C. R., and Liu, K. K.: A unique seasonal pattern in  
502 phytoplankton biomass in low-latitude waters in the South China Sea, *Geophys. Res. Lett.*,  
503 32, L08608, doi:10.1029/2004GL022111, 2005.

504 Wang, D. X., Liu, Y., Qi, Y. Q., and Shi, P.: Seasonal variability of thermal fronts in the northern  
505 South China Sea from satellite data, *Geophys. Res. Lett.*, 28, 3963–3966, 2001.

506 Webster, P. and Yang, S.: Monsoon and ENSO: Selectively interactive systems, *Q. J. Roy. Meteor.*  
507 *Soc.*, 118, 877-926, 1992.

508 Westberry, T., Behrenfeld, M. J., Siegel, D. A., and Boss, E.: Carbon-based primary productivity  
509 modeling with vertically resolved photoacclimation, *Global. Biogeochem. Cy.*, 22, GB2024,  
510 doi:10.1029/2007GB003078, 2008.

---

511 Yelland, M. J. and Taylor, P. K.: Wind stress measurements from the open ocean, *J. Phys.*  
512 *Oceanogr.*, 26, 541-558, 1996.

513 Yelland, M. J., Moat, B. I., Taylor, P. K., Pascal, R. W., Hutchings, J., and Cornell, V. C.: Wind  
514 stress measurements from the open ocean corrected for airflow distortion by the ship, *J. Phys.*  
515 *Oceanogr.*, 28, 1511-1526, 1998.

516 Zhang, C.Y.: Response of chlorophyll a to marine environment variability at multiple temporal  
517 scale in the Taiwan Strait. Ph.D., Xiamen University (China), 2006.

518 Zhang, C., Hu, C., Shang, S., Muller-Karger, F. E., Li, Y., Dai, M., Huang, B., Ning, X., and Hong,  
519 H.: Bridging between SeaWiFS and MODIS for continuity of chlorophyll-*a* concentration  
520 assessments off Southeastern China, *Remote. Sens. Environ.*, 102, 250-263, 2006.

521

522

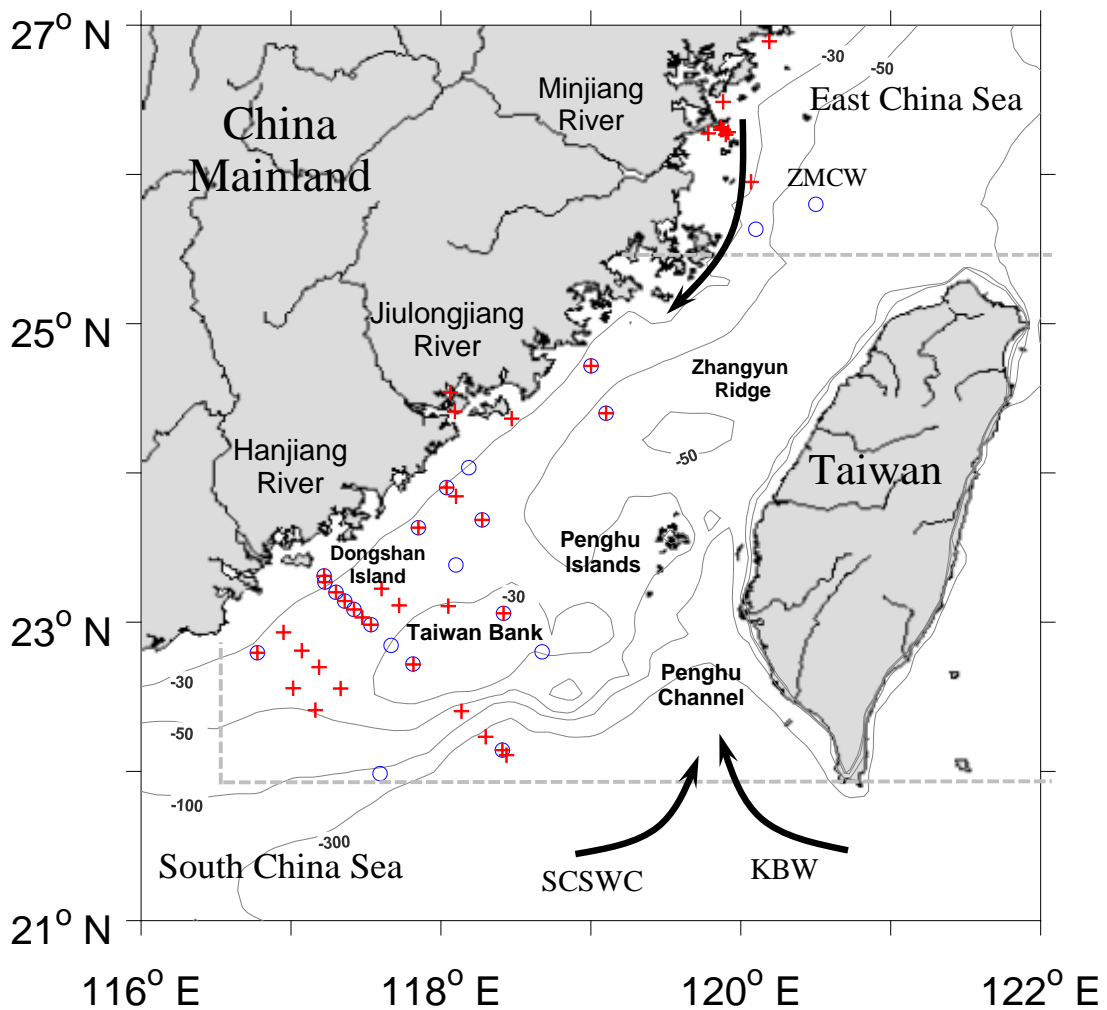
**Table 1** Symbols, abbreviations and description

Symbol	Description	Unit
ABI	Areal Bloom Index	$\text{m}^{-1}$
$a_{\text{ph}}$	Absorption coefficient of phytoplankton; $a_{\text{ph}}(412)$ means $a_{\text{ph}}$ at 412 nm; $a_{\text{ph}}(443)$ means $a_{\text{ph}}$ at 443 nm	$\text{m}^{-1}$
$A_{\text{ph}}$	$a_{\text{ph}}(443)$	$\text{m}^{-1}$
$a_{\text{t-w}}$	Total absorption without pure water contribution; $a_{\text{t-w}}(443)$ means $a_{\text{t-w}}$ at 443 nm	$\text{m}^{-1}$
Chl	Chlorophyll <i>a</i> concentration	$\text{mg/m}^3$
MEI	Multivariate ENSO Index	
QAA	Quasi-analytical Algorithm (Lee, et al. 2002)	
RMSE	Root mean square error	
$R_{\text{rs}}$	Remote sensing reflectance	$\text{sr}^{-1}$
TWS	Taiwan Strait	

**Table 2** Error statistics between derived and *in situ* absorption coefficients and Chl data\*

	Band (nm)	RMSE	RMSE_log	$\varepsilon$ (%)	$R^2$	n
Derived from field measured $R_{rs}$ (N=88)						
$a_{t-w}(\lambda)$	412	0.269	0.155	26.1	0.80	88
	443	0.197	0.135	23.1	0.87	88
	488	0.079	0.117	22.4	0.93	88
	531	0.040	0.169	37.7	0.91	88
$a_{ph}(\lambda)$	412	0.086	0.145	26.9	0.86	88
	443	0.093	0.150	28.0	0.87	88
	488	0.066	0.189	43.0	0.90	88
	531	0.051	0.348	116.1	0.85	88
Chl		5.067	0.429	162.0	0.80	88
Derived from MODIS $R_{rs}$ (N=30)						
$a_{t-w}(\lambda)$	412	0.076	0.150	25.9	0.76	30
	443	0.063	0.127	21.1	0.91	30
	488	0.021	0.109	20.2	0.91	30
	531	0.011	0.142	25.7	0.91	30
$a_{ph}(\lambda)$	412	0.078	0.252	36.1	0.87	25
	443	0.070	0.226	33.8	0.86	25
	488	0.019	0.265	34.8	0.87	28
	531	0.012	0.267	63.5	0.88	26
Chl		2.063	0.383	135.6	0.81	30

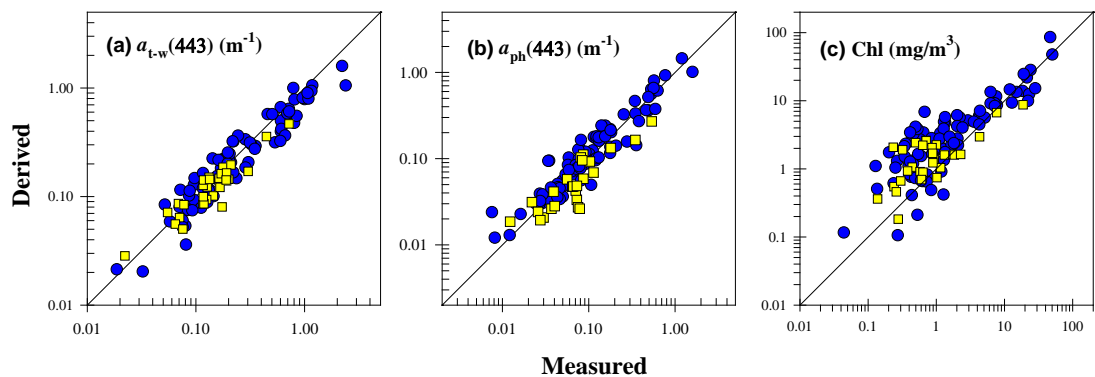
\* N is the number of data tested, while n is the number of valid retrievals.



530  
531

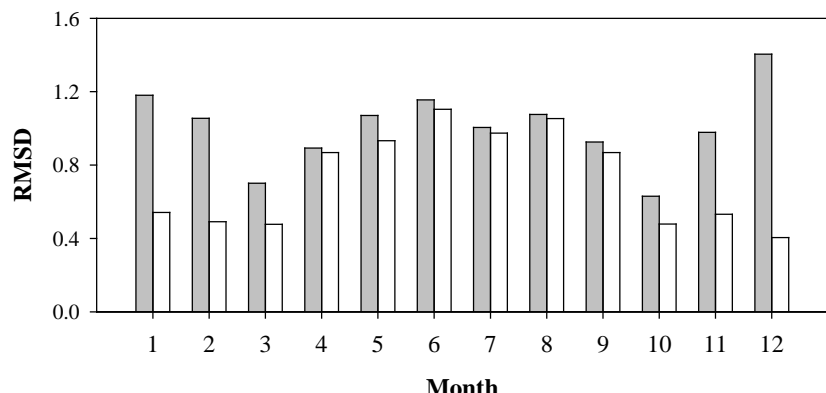
532 **Fig. 1** Map of the Taiwan Strait; ZMCW: Zhe-Min Coastal Water; SCSWC: South China Sea  
533 Warm Current; KBW: Kuroshio Branch Water; the red cross and blue circle symbols show the  
534 locations where field measured  $R_{rs}$  and MODIS  $R_{rs}$  have match-up *in situ* observed absorption  
535 coefficients, respectively; the grey lines indicate the boundaries of the research area of this study.

536



537

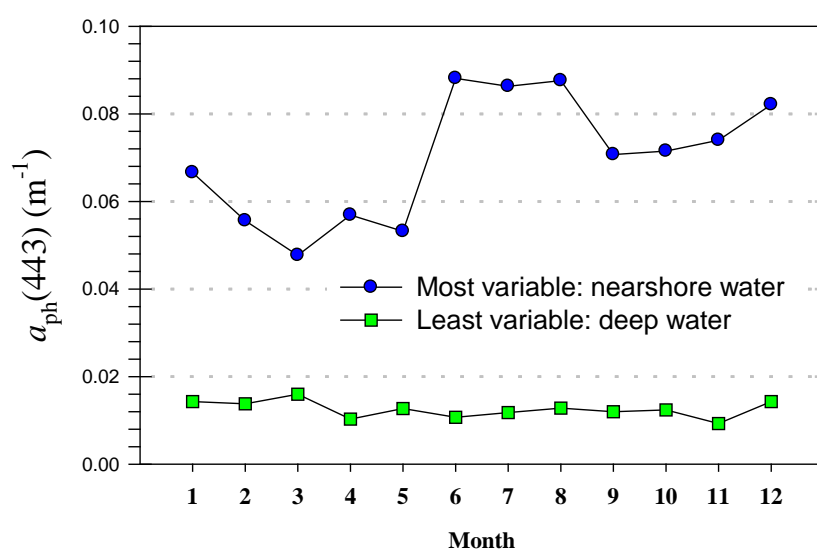
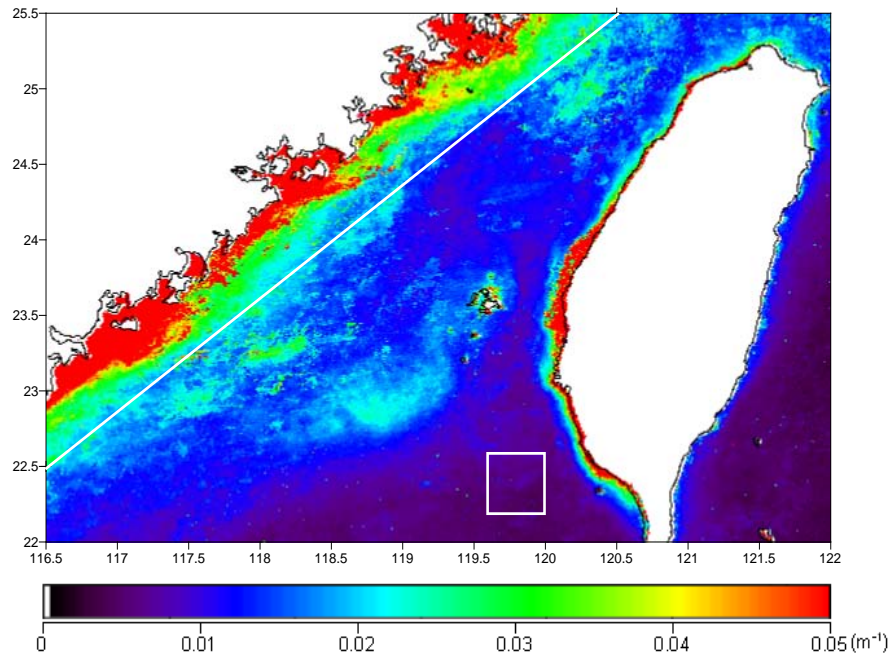
538 **Fig. 2** Scatter plot of  $R_{ts}$  (*in situ*: blue circles; MODIS: yellow squares) derived (a)  $a_{t-w}(443)$ ,  
 539 (b)  $a_{ph}(443)$  and (c) Chl versus field measured data.



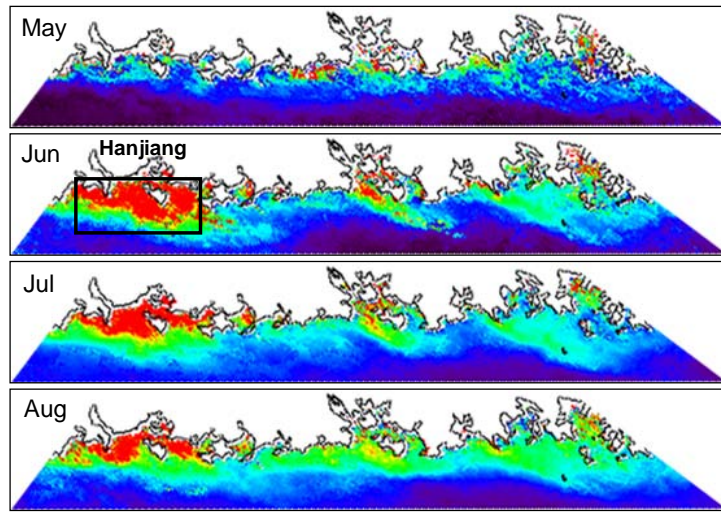
540

541 **Fig. 3** Root mean square deviation between normalized spatial anomaly of  $a_{ph}(443)$  and that of  
542 Chl (the grey bar), and normalized spatial anomaly of  $a_{t-w}(443)$  and that of Chl (the empty bar).

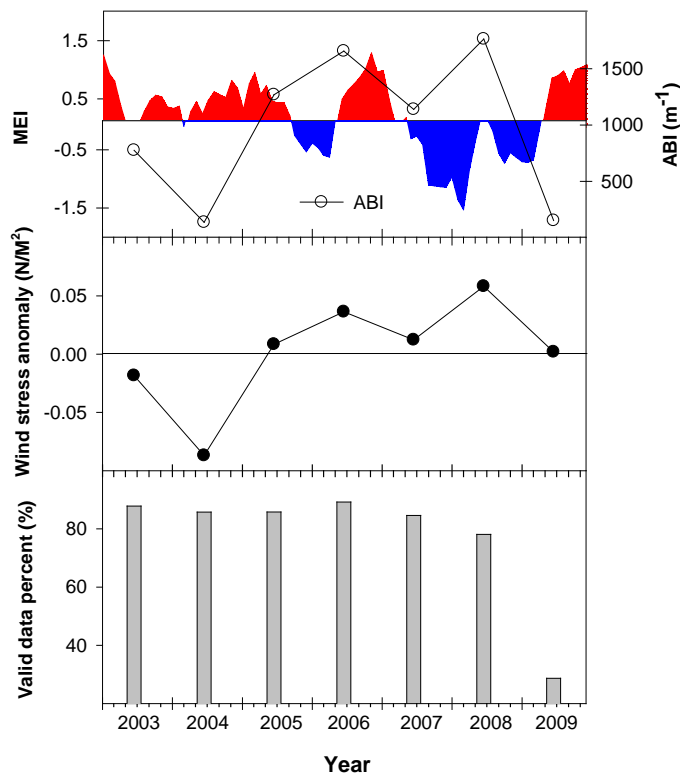
543



548 **Fig. 4** (a) Annual mean standard deviation of  $Aph$ ; (b) the annual cycle of  $Aph$  in the most  
 549 variable coastline (west of the white line alongshore on Fig. 4a) and least variable deep water(the  
 550 square at the right bottom of Fig. 4a) areas.

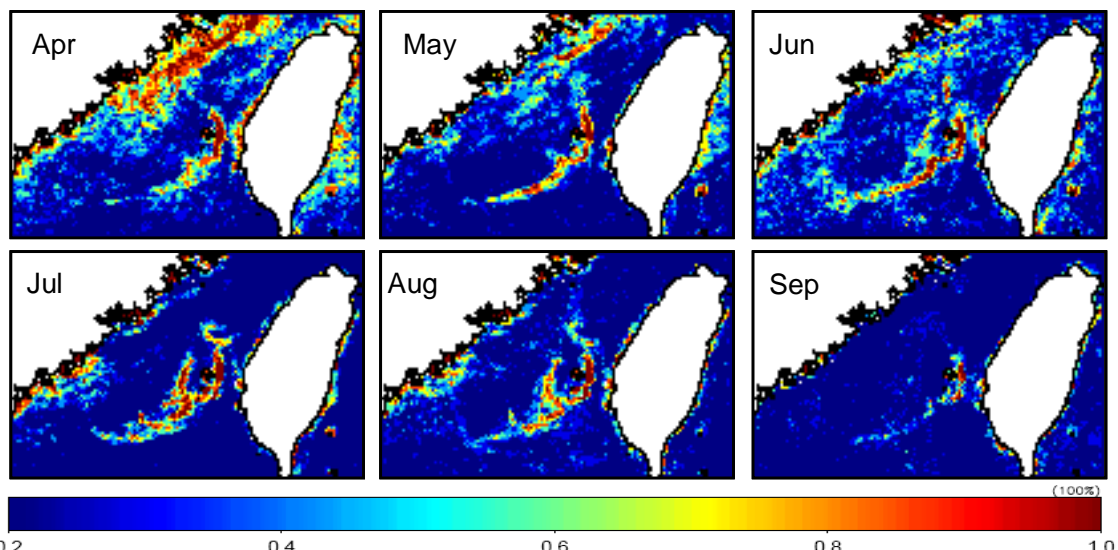
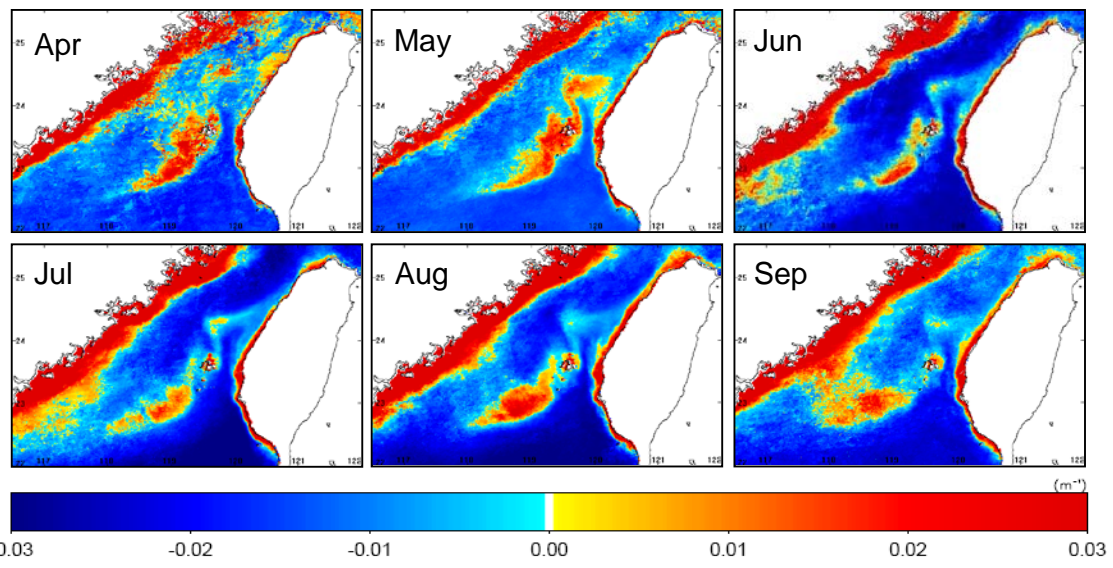


(a)



(b)

555 **Fig. 5** (a) close-up view of *Aph* in the nearshore water (west of the white line alongshore on  
 556 Fig. 4a) in May-August; (b) The interannual variation of *Aph* percentage of valid retrievals and  
 557 alongshore wind stress anomaly in the area of Hanjiang River estuary in June during 2003-2009  
 558 and the MEI.



565 **Fig. 6** (a) Spatial anomaly of *Aph* in the TWS in April-September; (b) thermal frontal  
566 probability in April-September.